Applied Thermal Engineering 230 (2023) 120649

Contents lists available at ScienceDirect

Applied Thermal Engineering

journal homepage: www.elsevier.com/locate/ate

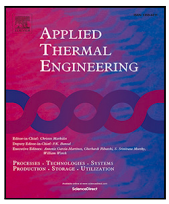

Research Paper

Numerically efficient two-step CFD simulation model of flow regime and heat transfer for hot water shower sterilizers☆

Elias Hashemian Nik *, Simon Pletzer, Christoph Hochenauer

Institute of Thermal Engineering, Graz University of Technology, Inffeldgasse 25b, Graz, 8010, Styria, Austria

ARTICLE INFO

Keywords:
Hot water shower sterilizer
Numerically efficient model
Heat transfer
Flow and film regime

ABSTRACT

This work was carried out to create a numerically efficient validated simulation model for Hot Water Shower (SWS) sterilizers. The goal of the work was to achieve a more homogeneous temperature and water distribution inside the sterilizers developed in the future. A lab-scale test bench of an SWS sterilizer with a configurable water volume flow rate and temperature was designed to validate the Computational Fluid Dynamics (CFD) model that was created. The heating and cooling phases at water volume flow rates of 20 and 40 m^3/h per m^2 spraying surface were analyzed. Additionally, the flow and film regime were studied. The CFD model was split into two simulation steps to significantly improve the numerical efficiency. The novel two-step approach developed is computationally 1800 times faster as compared with a complete sterilization cycle than a state-of-the-art approach. The simulated temperature of the test load was in good accordance with the experimental measurements. The flow regime was largely accurately replicated. Overall, the created validated CFD model is suitable for upscaling to an industry-sized SWS sterilizer due to its numerical efficiency.

1. Introduction

The proper sterilization of various products that directly or indirectly contribute to our daily lives is of immense importance. Sterilization makes it possible to adhere to extremely high safety standards and ensures high quality and repeatability in many industries. The most popular sterilization method is done by using various heating methods which are naturally very energy-demanding. The high energy demand of these sterilization devices underlines the importance of improving their energy efficiency. Needless to say, lower operating costs are an additional benefit that accompanies improved energy efficiency, especially with energy prices as high as they are today. Another relevant factor is process time. Achieving faster production times for pharmaceutical products can greatly improve profitability. Overall, there are both ecological and economic reasons for optimizing sterilizers.

This work directed a focus toward developing a numerically inexpensive model for Hot Water Shower (SWS) sterilization. This sterilization method is primarily used for the sterilization of completely closed, large-volume liquid products. The load is brought into the SWS sterilizer and heated by showering the products continuously with water that is heated by heat exchangers. The heated water acts as the sterilizing agent. The actual sterilization phase begins once the products have been completely heated to a specific temperature. Typically, the product temperature is held constant at a sterilization temperature of 121 °C. After the sterilization phase is finished, the circulating water is cooled to reduce the temperature of the products prior to their removal from the sterilizer [1].

The energy efficiency of SWS sterilizers can be increased by reducing the volume flow rate, which decreases the energy needed for water recirculation. Another important criterion for the energy efficiency is the homogeneous distribution of the sterilization agent and the temperature inside the sterilizer. This homogeneous distribution is critical, as it reduces the sterilization time to a minimum and ensures the required sterilization safety. Lastly, reducing the heat loss to the surroundings and the energy wasted through heating the sterilization device itself are further areas where optimization is possible. As increased computational power has become available, validated numerical simulations have become useful tools for technical optimization. These simulations can be used to evaluate various parameter changes without making cost-intensive and time-consuming modifications to the actual working devices. Thus, this study was carried out to provide a simple, robust, and numerically inexpensive model that would make optimizations of devices possible in the future.

Several previously published studies analyzed the energy efficiency of sterilizers and retorts using steam as the sterilizing agent. Simpson et al. [2] analyzed the energy demand of batch thermal processing and

☆ CFD model for SWS sterilizer.

* Corresponding author.
E-mail address: elias.hashemiannik@tugraz.at (E. Hashemian Nik).

https://doi.org/10.1016/j.applthermaleng.2023.120649
Received 29 November 2022; Received in revised form 22 March 2023; Accepted 24 April 2023
Available online 29 April 2023

Nomenclature

Variables

c_d	Drag coefficient
c_p	Specific heat capacity at constant pressure
d	Diameter
$\vec{F}$	Force
g	Gravitational acceleration
h	Heat transfer coefficient
k	Turbulent kinetic energy
k	Thermal conductivity
L	Characteristic length
m	Mass
p	Pressure
p_A	External aerodynamic pressure
p_I	Internal pressure
p_σ	Surface tension pressure
$\dot{q}$	Heat flux density
Re	Reynolds number
s_l	Film height
T	Temperature
t	Time
u_m	Mean velocity
$\vec{u}$	Flow velocity
$\hat{V}$	Surface-averaged volume flow rate
We	Weber number
$\overline{x}_t^{exp}$	Average experimental temperature data
y_t^{sim}	Simulation temperature data

Greek letters

ε	Turbulent dissipation rate
μ	Dynamic viscosity
ν	Kinematic viscosity
ρ	Density
σ	Surface tension of the film
τ	Relaxation time

Indices

d	Droplet
l	Liquid film
W	Wall
∞	Free stream conditions

Abbreviations

CFD	Computational Fluid Dynamics
DPM	Discrete Phase Model
EWF	Eulerian Wall Film
GCS	Grid Convergence Study
MAE	Mean Absolute Error
RANS	Reynolds-averaged Navier–Stokes
SHZ	Slowest Heating Zone
SWS	Hot Water Shower
TAB	Taylor Analogy Breakup
USB	Unified Spray Breakup
VOF	Volume of Fluid

identified possible energy savings of up to 15–25% by insulating the steam retort. Moreover, Lau et al. [3] developed a numerical model of a steam sterilizer using steady state correlations. Their model showed major heat losses through the walls, steam and air flow through the vents, and water overflow of 35%, 23%, and 8% respectively. Peesel et al. [4] developed concepts for improving the energy efficiency of the steam retort sterilization process, including preheating the products using waste heat, keeping the retort doors closed between sterilization processes, reusing the condensate, and recovering heat from the cooling water. Philipp et al. [5] developed a thermodynamic model for product batch sterilization that demonstrates an energy-saving potential of up to 83% when implementing heat recovery measures in such processes.

Numerous papers have experimentally or numerically analyzed the use of steam as the sterilizing agent inside sterilizers or retorts. Studies by Feurhuber et al. [6–11] presented capable numerical models to predict the steam flow, steam temperature, load temperature, steam quality, and inactivation of bacteria inside steam sterilizers. Folezzani et al. [12] performed validated multiphase Computational Fluid Dynamics (CFD) simulations of a full-sized steam retort sterilizer with and without trays focusing on the Slowest Heating Zone (SHZ) inside a product container. Several other studies investigated exclusively the heat transfer inside the products that are placed in steam sterilizers or retorts. Farid and Ghani [13] created a CFD model to predict the SHZ of liquid food in cans. Similarly, Kannan and Sandaka [14] analyzed the heat transfer inside canned foods.

Only a limited amount of research has focused specifically on sterilizers that utilize liquid water as the sterilizing agent. Cordioli et al. [15] created a CFD model for thermal treatment by spraying hot water on canned solid–liquid mixtures in the food industry. The simulation with the glass jars was performed by applying a simplified, experimentally obtained, time-varying temperature boundary condition. Mosna and Vignali [16] studied a CFD model of an overheated water spray retort sterilizer and validated the temperature of the test loads. This study included a multiphase simulation of both the autoclave domain containing a steam and water mixture and the product domain, but did not include an analysis of the flow and film regimes inside the sterilizer. Any insight into the distribution and behavior of the liquid phase inside such SWS sterilizers is currently lacking.

Visual observations inside the chamber of SWS sterilizers have shown that the water droplet sprays form liquid films on the loaded products. A numerically efficient method to model the falling droplets is presented by the Discrete Phase Model (DPM). The study of Cleary and Serizawa [17] provides an example of the use of the DPM to simulate water droplets. Many studies have analyzed the hydrodynamics of liquid films and the heat and mass transfer in falling films. The properties of the liquid film are critical to the heat transfer. Tahir and Al-Ghamdi [18] investigated the evaporation heat transfer process of falling films by using a two-dimensional Volume of Fluid (VOF) model. A similar three-dimensional VOF model was developed by Wang et al. [19]. A computationally less expensive method is the Eulerian Wall Film (EWF) model. Several studies have coupled the efficient EWF and DPM models for other applications such as combustion [20], supersonic condensation flows [21], and gasoline engines [22].

To the author's best knowledge, no published research is available on the numerical simulation of the flow regime and spatial distribution of the liquid phase coupled with an analysis of the heat transfer inside SWS sterilizers. The biggest challenge in this research area is the immense computation time and effort needed to model the multiphase flow of a representative section of an industry-sized SWS sterilizer. Thus, an extremely numerically efficient, simplified model is needed to make such a simulation feasible. The flow characteristics and the heat transfer mechanisms obtained by applying this model should also agree satisfactorily with experimentally obtained data. The influence of the water volume flow rate and the spatial distribution of the water were studied in this work. The ultimate goal was to utilize the model to examine a section of an industry-sized SWS sterilizer in order to improve its distribution quality and efficiency in the future.

This work, therefore, was carried out to achieve two main objectives:

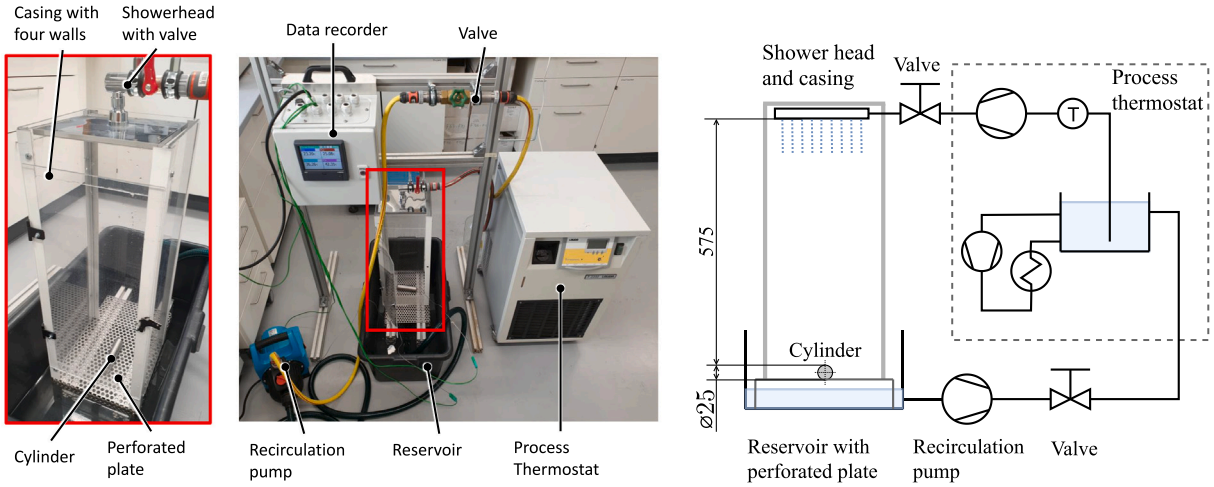

Fig. 1. Photographs and hydraulic diagram of the created lab-scale test bench. All dimensions are in mm.

- An experimental study was performed with a water shower test bench to gather measurement data to validate a CFD model. The data needed to include the flow regime and the temperature of the test load.
- An extremely numerically efficient unsteady CFD model was created to reproduce the flow regime of the test bench and accurately simulate the wall heat flux density on the surface of the test load. Shower heating and cooling needed to be accurately simulated, and the influence of different water volume flow rates to be determined.

2. Experimental study

The experimental study is critical for gaining a clear understanding of the general flow regime in the showering system. It additionally provides the data that are used to validate the test load temperature used in the simulation model. In this study, a simplified lab-scale test bench of an SWS sterilizer was built primarily to supply a configurable water volume flow rate and temperature to a nozzle grid above the test load. The test load could be heated or cooled depending on the configured water temperature. This test bench replicates a small representative section of an industry-scaled SWS sterilizer. Photographs and a hydraulic diagram of the test bench are displayed in Fig. 1. A stainless-steel cylinder of type 1.4301 with a length of 100 mm and a diameter of 25 mm was used as a test load. The cylinder was equipped with two sealed type-K thermocouples inserted into drilled holes at different depths along the cylinder symmetry axis (13 and 27 mm from the head surfaces, respectively, as indicated in Fig. 6). The cylinder was placed on a perforated plate as is common in an industry-sized sterilizer. The vertical distance between the nozzle grid and the perforated plate was 600 mm. Above the cylinder, the nozzle grid with a ten-by-ten grid and a nozzle diameter of 1.1 mm was mounted and connected to the water circulation cycle. The details of the nozzle grid setup are compared to the numerical model in Fig. 2. The setup was enclosed on its sides by acrylic glass. A process thermostat with a configurable pump pressure and internal heat exchanger was used to accurately heat or cool the circulating deionized water. Thus, in this study, the water could be pumped from the process thermostat to the nozzle grid at a desired volume flow rate and temperature. After the water had been collected in a reservoir, it was recirculated into the process thermostat by a recirculation pump.

The created test bench was used to analyze two different surface-averaged volume flow rates at 20 and 40 m^3/h per m^2 spraying surface. A surface-averaged volume flow rate was used to describe the volume flow rate in relation to the utilized spraying surface, which included the total area of the nozzle grid. This enabled us to make a direct comparison with industrial scale devices that have significantly larger spraying surfaces. The heating and cooling phases were evaluated for a period of 40 s each. In the heating phase, the cylinder with a homogeneous starting temperature of 25 °C was showered with water at a temperature of 50 °C. In the cooling phase, the cylinder with a homogeneous starting temperature of 80 °C was cooled with water at a temperature of 22 °C. The starting cylinder temperature was achieved by using a drying oven. The temperature levels chosen were lower than those used in the industrial process to avoid the demand for a pressure vessel; i.e., the lab-scale test bench was kept at atmospheric pressure. Additionally, the precise process thermostat used could not achieve a constant temperature higher than 50 °C; thus, this defined the upper limit of the water temperature in the heating scenario. The temperature data recorded by the thermocouples were logged during the experiments. For each scenario, at least three test runs were performed and recorded. The cylinder temperature was measured with an accuracy of ± 1.5 K, while the water temperature was controlled by the thermostat with an overall uncertainty of ± 0.6 K. The surface-averaged volume flow rate was kept within an overall uncertainty range of 15% from the desired value. The positioning and orientation of the cylinder were maintained throughout the three test runs for each scenario. The reproducibility of the results was good. Additionally, the flow regime was analyzed using the lab-scale test bench. The flow behavior of the droplets and the film was studied using high-speed photography and slow-motion videos. A particular emphasis was placed on the disintegration of the liquid jets, droplet breakup behavior, turbulent dispersion, and the film regime on the cylinder.

3. Development of the model

The processes that take place inside the test chamber represent a combination of the dynamics of sprays and heat transfer mechanisms. To the author's best knowledge, the process of SWS sterilization has never been replicated with a numerical model considering these aspects before. In this section, the different physical effects and the utilized numerical model approaches or simplifications are discussed. The model was created in the CFD software ANSYS Fluent 2022.

3.1. Multiphase model

The utilized DPM is based on the Euler–Lagrange approach. The fluid phase (i.e., air in this case) is calculated as a continuum by solving the basic equation of fluid mechanics. A turbulent flow for the

continuous phase was determined based on an approximated Reynolds number Re of $1.2 \cdot 10^4$ as defined in Eq. (1) [23]

$$Re = \frac{u_m\, L}{\nu} \tag{1}$$

where L is the characteristic length, u_m is the mean velocity of the fluid, and ν is the kinematic viscosity. The most common and computationally efficient approach for solving industrial turbulent flow problems is to apply the Reynolds-averaged Navier–Stokes (RANS) models. The $k-\varepsilon$ model with the Enhanced Wall Treatment model was chosen out of several different RANS models available [24].

The dispersed phase is solved by tracking a large number of droplets that travel through the flow field. Exchange of momentum, mass, and energy between the dispersed and fluid phases is possible. The trajectories of the droplets are calculated at specified time intervals by integrating the force balance on the droplet as shown in Eq. (2) [25]

$$m_d \frac{d\vec{u}_d}{dt} = m_d \frac{\vec{u}-\vec{u}_d}{\tau_d} + m_d \frac{\rho_d - \rho}{\rho_d}\vec{g} + \vec{F}_{other} \tag{2}$$

where m_d stands for the droplet mass, $\vec{u}$ is the fluid phase velocity, $\vec{u}_d$ is the droplet velocity, ρ is the fluid density, ρ_d is the density of the droplet, $m_d \frac{\vec{u}-\vec{u}_d}{\tau_d}$ is the drag force, $\vec{F}_{other}$ stands for any additional forces, and τ_d is the droplet relaxation time [26] as defined in Eq. (3)

$$\tau_d = \frac{\rho_d d_d^2}{18\mu} \frac{24}{C_d Re_d} \tag{3}$$

where μ is the molecular viscosity of the fluid, C_d is the drag coefficient, d_d is the droplet diameter, and Re_d is the droplet Reynolds number.

3.2. Disintegration of liquid jets

When a jet of liquid exits a nozzle in a continuous cylindrical shape, the cohesive and disruptive forces on the surface compete against each other, leading to oscillations and perturbations. Under favorable circumstances, the oscillations are amplified, and the continuous jet stream disintegrates into smaller droplets. This is referred to as primary atomization. The further breakup of droplets is called secondary atomization. In flow regimes such as those that occur in SWS sterilizers, axisymmetric disturbances as well as the characteristic dumbbell shape just before the breakup are visible in the breakup. The pinching at the end of the jet stream causes it to become unstable and break up into smaller droplets. The created droplets may coalesce, forming larger droplets with smaller single satellite droplets in between [27].

To reduce computational effort, the formal disintegration of the liquid jets (e.g. using the VOF model) was omitted. Instead, the droplets were directly injected using the DPM. To determine the velocity of the droplets after the jet stream disintegration, the droplet velocity at the test bench was measured using slow-motion videos and a length scale. To achieve experimentally matching volume flow rates and inlet velocities for the droplets, the inlet diameter was changed accordingly. This change ensured the condition of the droplets shortly after the actual nozzle without simulating the actual disintegration.

3.3. Droplet breakup and dispersion

In an equilibrium, the internal pressure at any point on the droplet surface p_I equals the external aerodynamic pressure p_A and the surface tension pressure p_σ leading to Eq. (4) [28].

$$p_I = p_A + p_\sigma = constant \tag{4}$$

A droplet remains stable if any change in p_A can be compensated by a change in p_σ to keep p_I constant. If p_A is too large and cannot be compensated by a change in p_σ, the droplet may deform, causing a further reduction in p_σ and eventually its breakup into smaller droplets. Generally, the breakup of droplets is determined by dynamic pressure, surface tension, and viscous forces. The type of deformation and breakup partly depends on the physical properties of the liquid and gaseous phases and the flow pattern around the droplet [28].

Several analytical models, including the Taylor Analogy Breakup (TAB) model, Droplet Deformation Model, and the Unified Spray Breakup (USB), were described in detail by Chryssakis et al. [29]. Generally, these are used to model the transformation of the bulk liquid into the resulting droplets based on the influence of the external forces of the pressure or surface shear [28]. The TAB model was used for the numerical model created in this study. The turbulent dispersion was modeled by applying the stochastic tracking (random walk) model [26]. This represents one way to model the dispersion of the droplets based on turbulence in the fluid phase. It also enables the user to consider the effect of instantaneous turbulence velocity fluctuations on the droplet trajectories by applying stochastic methods. The concept of the integral time scale is used, which is proportional to the droplet dispersion rate. Increasing the time scale translates to more turbulent motion within the flow. The time scale constant was set at 0.9 based on experimental observations.

3.4. Film regime

Some water droplets released within the test bench will eventually hit the cylinder after they have been ejected from the nozzles and traveled through the air. When they collide with the cylinder, they are expected to form a liquid film. A film model is made up of a two-dimensional thin film which forms on a wall surface when liquid droplets impinge the surface. The possible outcomes of the impingement include sticking, rebounding, spreading, and splashing. Flow separation and sheet breakup are possible as well. Another important mechanism is the heat conduction with the wall and the convective heat transfer.

The EWF model interacts with the DPM through the source terms of the film equation. The discrete droplets defined in the DPM are collected to form the wall film. Additional discrete droplets can be formed when the film separates or is stripped from the wall. According to the work by Friedrich et al. [30], the separation of the wall film occurs when a critical angle is exceeded and the Weber number based on the liquid film We_l is above a minimum value. The Weber number is defined in Eq. (5), where σ is the surface tension of the film, ρ_l is the film density, s_l stands for the film height, and $\vec{u}_l$ denotes the film velocity.

$$We_l = \frac{\rho_l\, s_l\, |\vec{u}_l|^2}{\sigma} \tag{5}$$

For the energy transfer equation for the film, the energy flux from the gas side as well as the energy flux from the wall side must be considered. DPM coupling with the EWF model was used in the created model. The partial wetting of the film was modeled as described by Meredith et al. [31]. The applied sub-models include gravity force, surface tension, surface shear force, spreading term, and edge separation. The critical Weber number was set to 0.025 and the critical angle to 11°. The surface contact angle for the polished cylinder walls was set to 77° according to Xu et al. [32]. The impingement model of Kuhnke [33] was used to determine the DPM interaction.

3.5. Geometry and mesh

The geometry for the numerical model was created based on a section of the lab-scale test bench. This section represents a sub-domain of an industry-scaled sterilizer that should be investigated in the future. The geometry consists of two volumes: a fluid volume representing the ambient air and a solid volume representing the steel cylinder. The ambient volume is enclosed by walls on the sides and the cylinder is located near the bottom surface of the ambient volume as shown in Fig. 2. A figure of the simulation domain is overlayed on a photograph of the actual test bench. In the experiments, the cylinder was positioned

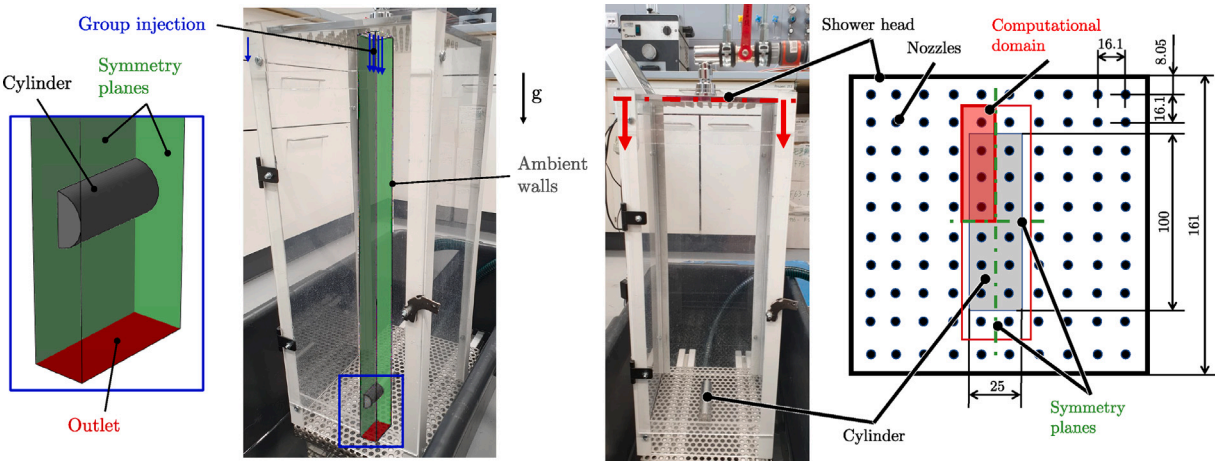

Fig. 2. Geometry of simulation model. All dimensions are in mm.

Table 1
GCS of three different cell meshes for the one-step cooling scenario with a volume flow rate of 40 m^3/h per m^2.

Mesh	Coarse	Medium	Fine
Cell number	11,000	26,000	121,000
Rel. sim. time	–	1x	4.5x
MAE TC1 in K	–	1.60	1.89
MAE TC2 in K	–	0.52	0.86

on the perforated plate, but the latter is not part of the simulated geometry. Two symmetry planes split the cylinder and the ambient volume into four quarters, only one-quarter of which had to be simulated. The computational domain for the unsteady model only includes four group injections as indicated in the top-down view shown in Fig. 2. Initial experiments showed that simulating only one row of nozzles inside the computational domain shown was sufficient, since further rows did not affect the wall film.

A relatively coarse poly-hexacore mesh with a finer boundary layer at the cylinder wall was generated for the ambient domain. A polygon mesh was used for the cylinder domain. The mesh used for the simulation consists of around 26,000 cells. The Mean Absolute Error (MAE) was used to calculate the error of the temperature simulation results y_t^{sim} and compared with the experimental data averaged over the three runs $\overline{x}_t^{exp}$. The MAE is formed as shown in Eq. (6) by calculating the sum of absolute errors divided by the number of time steps (21). In this case, a data point was recorded every two seconds throughout the whole flow time of 40 s. The average temperature measurement $\overline{x}_t^{exp}$ of one time step every two seconds in the three separate experimental runs was taken as a benchmark for all MAE calculations.

$$MAE = \frac{\sum_{t=0}^{40} |y_t^{sim} - \overline{x}_t^{exp}|}{21} \tag{6}$$

A Grid Convergence Study (GCS) was conducted to demonstrate the independence of the utilized cell mesh. The properties of and results for a comparatively coarse, medium, and fine mesh are shown in Table 1. The results shown in the table are from the cooling scenario with a volume flow rate of 40 m^3/h per m^2. The comparison of the complete temporal temperature profile is also shown in Fig. 7. The simulation with the coarse mesh showed divergent results. The fine mesh did not offer a lower error margin than the medium mesh, even though the simulation time was 4.5 times as long. Therefore, out of the three meshes presented in Table 1, the medium mesh was used for this work.

The DPM injections were positioned as shown previously in Fig. 2. The bottom surface of the ambient volume was set to a pressure outlet. The two symmetry planes were set to symmetry. The remaining ambient and all cylinder surfaces were defined as walls. The water volume flow rate was established at 20 and 40 m^3/h per m^2 spraying surface, and the water temperature, at 22°C or 50°C, depending on whether the cooling or heating period was simulated. The starting temperature of the cylinder was 80°C or 25°C for the cooling and heating phases, respectively. The diameter of the injections was set at 1.15 and 1.25 mm for the 20 and 40 m^3/h per m^2 settings, respectively. The diameter was defined so that the starting droplet velocity of the simulation matched the experimentally obtained velocity data. Thus, a computationally more expensive method of modeling the droplet behavior such as jet disintegration was avoided.

3.6. Numerical setup

The ambient volume was defined as air and the cylinder was defined based on the corresponding material properties, including ρ, c_p, and k. The energy equation was activated, and the gravitational force was configured. A pressure-based solver was used in the simulation model. The transient simulations were performed in time steps of 0.001 s. A SIMPLE scheme was used. “Second Order Upwind” was used for spatial discretization except for pressure where “PRESTO!” was configured. The transient formulation was set at “Bounded Second Order Implicit”.

It is possible to utilize the model as described above for the full flow time of 40 s. However, this incurs significant computational costs when the simulation is stretched over the whole sterilization process, which amounts to roughly 60 min of flow time. Therefore, the simulation needed to be optimized. This led to the development of a two-step approach. For the first simulation step, the mesh and all model settings were used as described earlier. The first step of the simulation required only a total of 2 s of flow time in this case. In the first 1.5 s, the flow regime was developed and the next 0.5 s were used for data collection. Statistical data sampling was used to create local time-averaged heat flux density and wall temperature variables. This enabled the calculation of a time-averaged local heat transfer coefficient for every cell of the cylinder wall by using a custom field function based on Eq. (7). The free stream temperature T_∞ was defined as the inlet water temperature.

$$h = \frac{\dot{q}_W}{(T_W - T_\infty)} \tag{7}$$

After 2 s of flow time had elapsed, the heat transfer coefficient could be profiled and imported into another model for the second simulation step. Here, the ambient volume domain was completely deactivated as well as the DPM and the EWF model. Only the cylinder domain with a very low cell count remained. A convection boundary condition is given for all cylinder wall cells by using the previously imported heat transfer coefficient. The second simulation step was used to complete the remaining 38 s of the total 40 s flow time. The

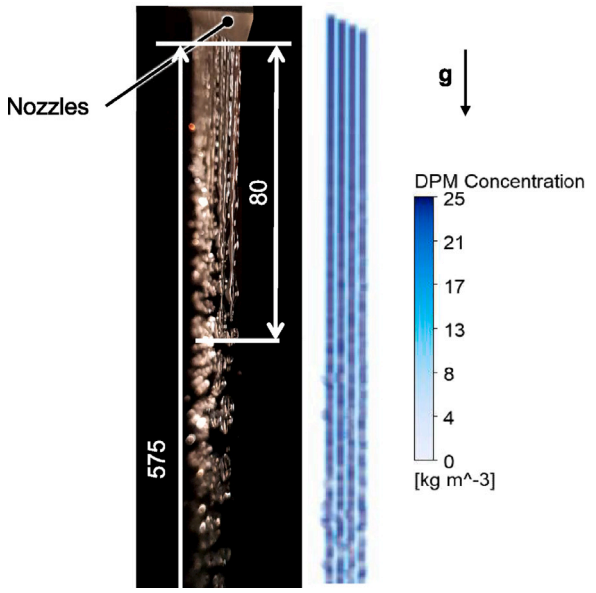

Fig. 3. Jet stream breakup into droplets during the experiment and simulation at 40 m^3/h per m^2. All dimensions are in mm.

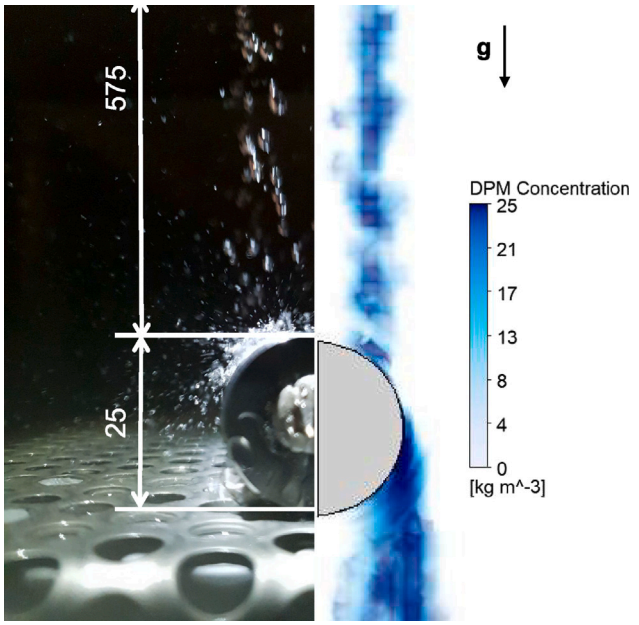

Fig. 4. Turbulent dispersion of experiment and simulation at 40 m^3/h per m^2. All dimensions are in mm.

required computational time for the second step can be neglected when compared to the multiphase simulation time required for the first step. To upscale the process to fit an industry-sized sterilizer, a longer process time without a constant free stream temperature T_∞ is needed. Here, a time-based function for the free stream temperature T_∞ needed to be implemented to consider the varying water temperature determined by the heat exchanger. Whereas the computational time in the shorter simulation of the lab-scale test bench was reduced by a factor of 20, a reduction factor of 1800 could be achieved over a whole process time of 60 min.

4. Results and discussion

In this section, the flow regime and temperature at the two measurement points are discussed. The results of the CFD simulations are shown and validated against the recorded experimental data collected with the lab-scale test bench.

4.1. Flow regime

Volume renderings showing the DPM concentration are displayed for the area near the inlet nozzles and the area of impact shown in Figs. 3 and 4. The left side of each figure depicts the experiment, and the right side depicts the simulation result. When the water exits a nozzle, a jet is formed. Applying the principle of mass conservation, a bigger diameter for a given volume flow rate translates to a lower flow velocity. Photos taken with high-speed photography and length scales were used to study how the jet stream broke up into droplets. The disintegration of the streams happens after 80 and 40 mm for a volume flow rate of 40 and 20 m^3/h per m^2, respectively. Additionally, the droplet breakup and turbulent dispersion behavior are of interest. During the remaining falling distance, the droplets may separate or collide with each other. The mean diameter of the droplets formed at the respective volume flow rates of 40 and 20 m^3/h per m^2 were measured at around 1.25 and 1.15 mm, respectively. As the falling height increases, the droplets are increasingly widely dispersed. As shown in Fig. 4, the simulation of the turbulent dispersion of the droplets is in good agreement with the experimental results.

The film thickness and the droplet velocity in the simulation for the two different volume flow rates at a random time step are shown in Fig. 5. The contour plots of the momentary time step show how the film parcels spread out. A repeating dynamic of the film regime was observed both in the experiments and the simulations. The previously discussed two-step approach takes advantage of this property. On multiple spots, larger accumulations of the film parcels took place. The scenario with a smaller volume flow rate shown in Fig. 5a shows less coverage of the cylinder head surface with liquid film than in Fig. 5b. The separation of the film parcels from the cylinder happened primarily at the midsection plane of the cylinder. This is partly following the observations of the flow behavior on the actual test bench. The simulation model, however, did not show the separation of the parcels at the bottom of the cylinder. The chosen modeling approach inherently comes with this limitation, but it is extremely numerically efficient, and the agreement between the simulated and experimental temperature data is good, as demonstrated in the next sections.

4.2. Temporal temperature profile

The results of the temperature measurements of the three experimental runs are compared to the simulation results in Fig. 6. The recorded data points of the three experimental runs include error bars which indicate the accuracy of the thermocouples. As two thermocouples were used, a total of six measurement points were plotted for each 2-s time step. TC2 was placed deeper inside the cylinder than TC1, as indicated in Fig. 6.

The experimental data points for the cooling scenario in Fig. 6a at 40 m^3/h per m^2 show only a small temperature decrease within the first two seconds. After the first two seconds, the recorded temperatures dropped significantly. A small delay in the temperature reading at the thermocouples is expected due to their inertia. It is apparent that the temperature measured at TC1, which was placed not as deep inside the cylinder as TC2, started to drop quicker than at TC2. This was attributed to the cooling effect of the cylinder head surfaces. After 40 s, both thermocouples recorded a temperature of around 25 °C. The simulated temperature matches the experimental data almost throughout the period within the measurement accuracy of the thermocouples. The biggest difference between the simulated and the experimental data is noted at the beginning of the cooling period. In this phase, the simulation data from TC1 and TC2 are virtually the same, whereas the

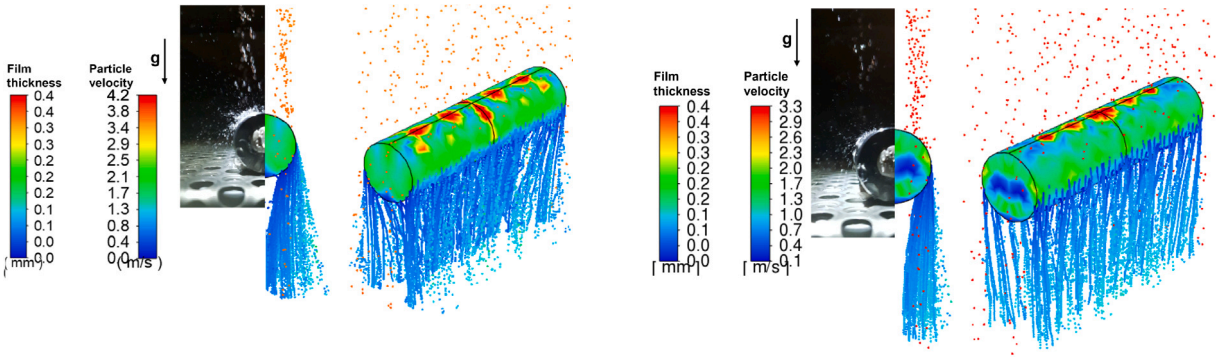

(a) at 40 m^3/h per m^2. (b) at 20 m^3/h per m^2.

Fig. 5. Wall film thickness and droplet velocity at different volume flow rates of simulation next to photos taken with high-speed photography of experiment.

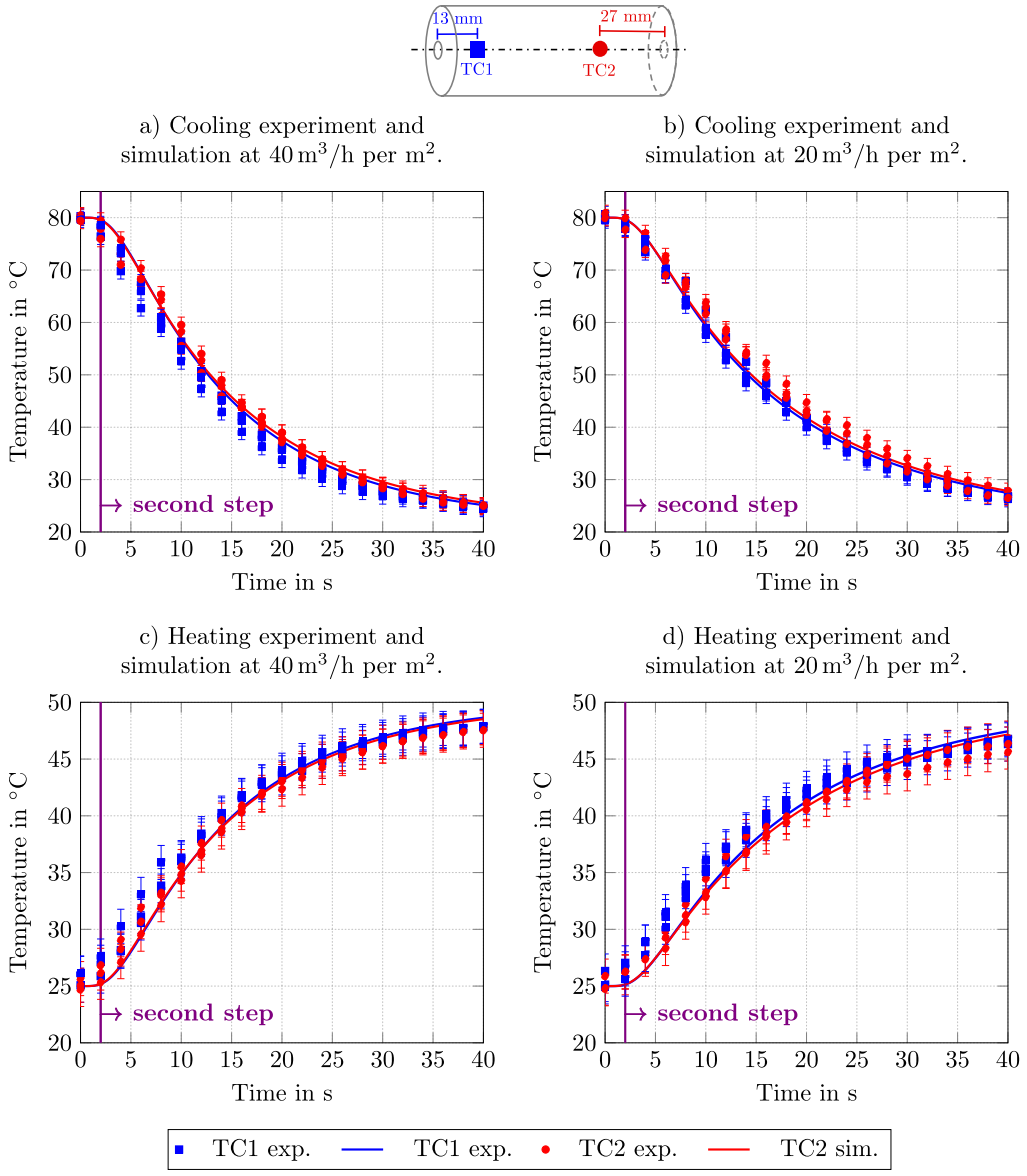

Fig. 6. Temperature plots of three runs of the heating and cooling experiment and the simulation at different water volume flow rates. The water temperature was 50 °C and the starting temperature of the cylinder was 25 °C during the cooling phase. The water temperature was 80 °C and the starting temperature of the cylinder was 22 °C during the heating phase. Error bars indicate the range of accuracy for the thermocouples.

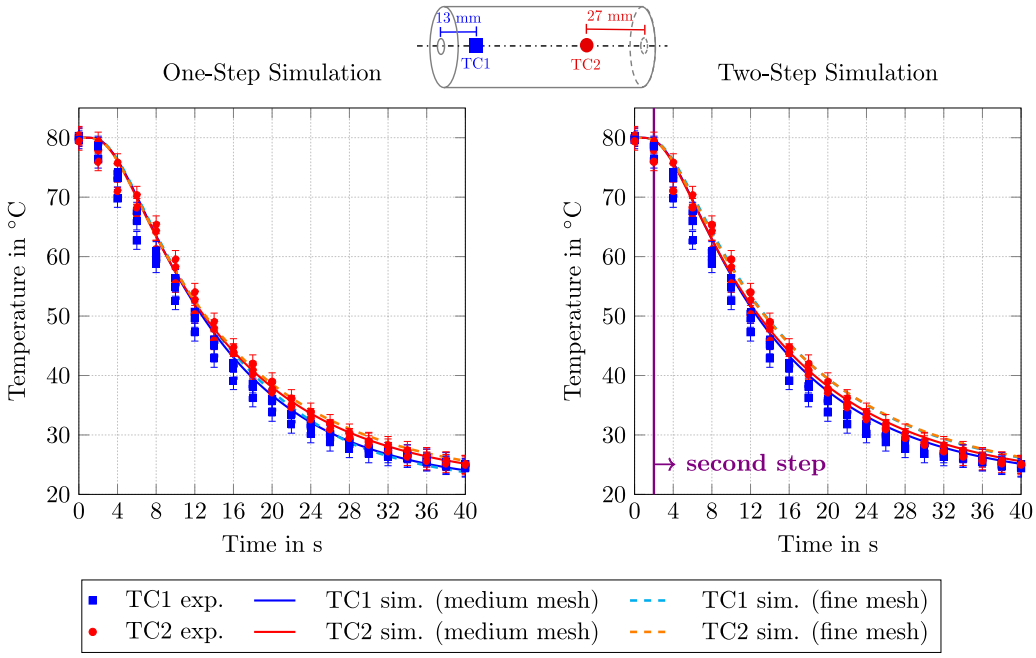

Fig. 7. Temperature plots of three runs of the cooling experiment and the unsteady one-step and two-step simulation with a water volume flow rate of 40 m^3/h per m^2 and a water temperature of 22 °C. The starting temperature of the cylinder was 80 °C. Error bars indicate the range of accuracy for the thermocouples.

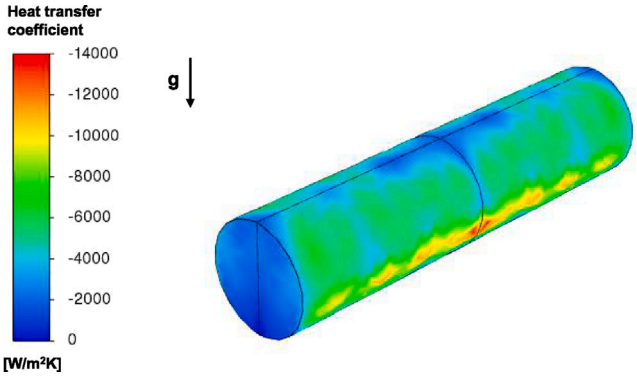

Fig. 8. Average heat transfer coefficient for the boundary condition of the cooling simulation at a volume flow rate of 40 m^3/h per m^2.

differences in the experimental data from TC1 and TC2 become apparent much earlier. Still, the absolute difference is small throughout the whole 40 s period. After 40 s of flow time, the simulated temperature is only 0.5 K lower than the mean measured value for TC1 and 0.6 K lower for TC2. The MAE accounts to 1.8 K for TC1 and 0.7 K for TC2.

The next scenario, shown in Fig. 6b, depicts the same cooling period at the lower volume flow rate of 20 m^3/h per m^2. As expected, the temperature of the cylinder dropped slower than in Fig. 6a. The stronger cooling of TC1 compared to TC2 was still noticeable. After 40 s, both experimental measurement points showed a temperature of about 27 °C, which is only 2 K above the end values when a volume flow rate of 40 m^3/h per m^2 was used. Again, almost the whole simulated temperature line matches the experimental data within the measurement accuracy range. The simulation data matches the effect of the increased volume flow rate well. After 40 s of flow time, the simulated temperature was only 0.6 K lower than the mean measured value at TC1 and 0.7 K at TC2. The MAE accounts for 0.7 K at TC1 and 1.3 K at TC2.

Fig. 6c shows the results of the heating simulation and experiment at the higher volume flow rate of 40 m^3/h per m^2. The general characteristics, albeit inverted, of the heating curve appeared to be the same as those of the cooling curve. The temperature measured at both thermocouples after 40 s was about 47.5 °C. The simulation seems to slightly underestimate the temperature at the beginning and slightly overestimate it at the end. The absolute difference is still extremely small. After 40 s of flow time, the simulated temperature was 0.8 K higher than the mean measured value at TC1 and TC2. The MAE accounts at 0.9 K for TC1 and 0.5 K at TC2.

A similar conclusion can be drawn from examining Fig. 6d, which shows the heating phase at the smaller volume flow rate of 20 m^3/h per m^2. Again, the temperature change is slightly weaker as compared to that seen at the higher volume flow rate. The temperature measured at both thermocouples after 40 s is about 47 °C. This is only 0.5 K lower than in the scenario with the higher volume flow rate of 40 m^3/h per m^2. The experimental data match these data closely. Although in this case, the same trend with a slight underestimation at the beginning and a slight overestimation of the heat transfer at the end can be seen, as shown in Fig. 6c. After 40 s of flow time, the simulated temperature was 0.7 K higher than the mean measured value at TC1 and 0.5 K higher at TC2. The MAE accounts at 1.2 K for TC1 and 0.5 K at TC2.

The effect of implementing the two-step approach on the temperature results is shown in Fig. 7. The results for the cooling scenario at 40 m^3/h per m^2 are compared to the results of a continuous one-step multiphase simulation with a flow time of 40 s.

The temperature lines observed for the one-step and the two-step simulations are extremely similar. The MAE of the one-step and two-step simulations for the chosen scenario are shown in Table 2. The MAE of the two-step simulation is almost the same as that of the one-step simulation. The comparisons between the other studied scenarios are not further discussed. The difference between the one-step and two-step models in these cases was similar to that seen in the scenario described above. Taking the novel two-step approach not only provided significant savings in terms of simulation time, but resulted in an excellent agreement between the simulation and experimental data.

The calculated average local heat transfer coefficient for this scenario is shown in Fig. 8. The illustrated state of the heat transfer coefficient determines the boundary condition for the second step of the simulation. The highest heat transfer coefficient can be found in the area of the film separation on the sides of the cylinder.

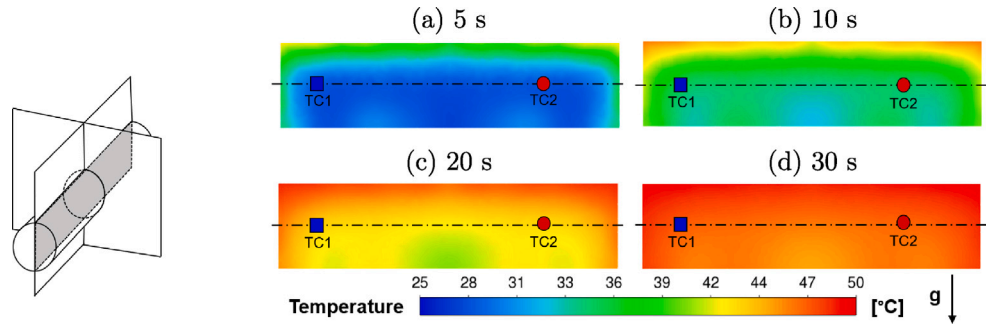

Fig. 9. Temperature contour on axial cylinder symmetry plane for the heating simulation at a volume flow rate of 40 m^3/h per m^2 and different time steps.

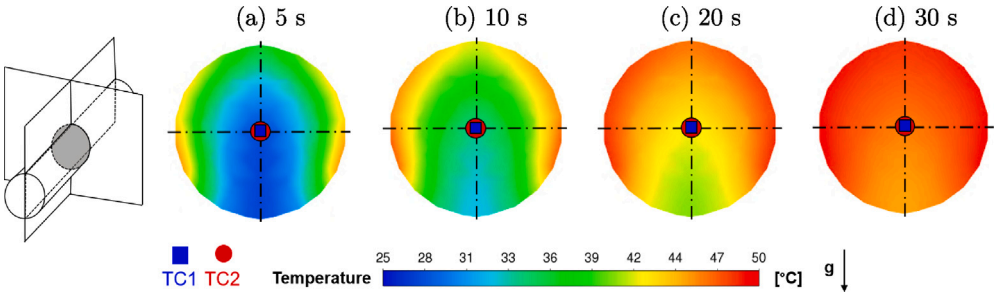

Fig. 10. Temperature contour on the radial cylinder symmetry plane for the heating simulation at a volume flow rate of 40 m^3/h per m^2 and different time steps.

Table 2
MAE of one-step and two-step simulations of the cooling simulation at a volume flow rate of 40 m^3/h per m^2.

	MAE TC1 (K)	MAE TC2 (K)
One-step sim.	1.6	0.5
Two-step sim.	1.8	0.7

4.3. Spatial temperature profile

The temperature profile inside the product is especially important in the heating phase. Ideally, the heating phase should be kept as short as possible to minimize the process time and heat losses. To achieve this, the behavior of the film regime on the products is important. If any spots are not covered sufficiently by a film of liquid, the heating time increases; these may also potentially impose a safety risk due to improper sterilization.

In Fig. 9, the temperature contour plot on the axial symmetry plane of the cylinder is examined during the heating phase at a volume flow rate of 40 m^3/h per m^2 and the different time steps of 5, 10, 20, and 30 s. This examination of the temperature distribution shows how the heating in this symmetry plane takes place primarily at the top of the cylinder and on the head surfaces. The contour plot after 30 s reveals a nearly homogeneous temperature profile.

The temperature contour for the same scenario on the radial cylinder symmetry plane is plotted in Fig. 10. Here, it can be seen that the strongest heating effect takes place at the sides of the cylinder where most of the film parcels are separated. As can be seen in Figs. 9 and 10, the SHZ of the cylinder throughout the simulation is located at the bottom where both symmetry planes overlap. The location of the SHZ can be explained by the early separation of the film on the sides of the cylinder.

5. Conclusion

In this study, a novel approach was proposed for a CFD model to replicate the flow and heat transfer mechanisms of SWS sterilizers. The two-step unsteady simulation model developed produced results that were in close agreement with the experimental data gathered with a lab-scale test bench. The use of a numerically efficient modeling approach is necessary to upscale the model and apply it to a section of an industry-sized sterilizer. The developed model enables the numerical efficiency needed to be obtained by combining the numerically inexpensive DPM and EWF model with a two-step approach, which significantly reduces the actual computation time needed to perform the multiphase simulation. This model provides more insight into processes occurring inside SWS sterilizers and serves as a tool for optimizing these devices in the future. This simplified approach is limited by certain limitations imposed by the wall film model and the omission of the jet disintegration at the nozzles. The position of the separation of the wall film was not fully replicated, and experimental data was needed to omit the jet disintegration.

The following conclusions can be drawn from this work:

1. The created lab-scale test bench could be utilized to gather temperature data for the validation of unsteady numerical models with different operating parameters. The effects of the film coverage and the volume flow rate were measured. The flow regime could be studied using high-speed photography and slow-motion videos.
2. Combining the DPM and EWF provided a well-suited, numerically efficient method that could be used to replicate the flow regime and heat transfer mechanisms that take place inside SWS sterilizers.
3. Significant amounts of computational time can be saved by splitting up the simulation into an initial flow development step and a second step with a convective boundary condition using a time-averaged heat transfer coefficient. This study proved that the simulation results, nevertheless, agree closely with experimental results. Throughout the total sterilization process, the two-step approach is 1800 times faster than the conventional one-step approach.

CRediT authorship contribution statement

Elias Hashemian Nik: Conceptualization, Methodology, Validation, Formal analysis, Investigation, Writing – original draft, Visualization. **Simon Pletzer:** Conceptualization, Methodology, Writing – review & editing. **Christoph Hochenauer:** Conceptualization, Methodology, Resources, Writing – review & editing, Supervision, Funding acquisition.

Declaration of competing interest

The authors declare that they have no known competing financial interests or personal relationships that could have appeared to influence the work reported in this paper.

Data availability

The authors do not have permission to share data.

References

[1] K. Banerjee, P.N. Cheremisinoff, Sterilization Systems, Technomic Publishing Company, Lancaster, PA, 1985.

[2] R. Simpson, C. Cortés, A. Teixeira, Energy consumption in batch thermal processing: model development and validation, J. Food Eng. 73 (3) (2006) 217–224, http://dx.doi.org/10.1016/j.jfoodeng.2005.01.040.

[3] W.L. Lau, J. Reizes, V. Timchenko, S. Kara, B. Kornfeld, Numerical modelling of an industrial steam–air sterilisation process with experimental validation, Appl. Therm. Eng. 75 (2015) 122–134, http://dx.doi.org/10.1016/j.applthermaleng.2014.09.031.

[4] R.-H. Peesel, M. Philippa, G. Schumma, J. Hesselbacha, T.G. Walmsleyb, Energy efficiency measures for batch retort sterilization in the food processing industry, Chem. Eng. Trans. (CET) 52 (2016) http://dx.doi.org/10.3303/CET1652028.

[5] M. Philipp, G. Schumm, P. Heck, F. Schlosser, R.-H. Peesel, T.G. Walmsley, M.J. Atkins, Increasing energy efficiency of milk product batch sterilisation, Energy 164 (2018) 995–1010, http://dx.doi.org/10.1016/j.energy.2018.09.002.

[6] M. Feurhuber, A. Cattide, M. Magno, M. Miranda, R. Prieler, C. Hochenauer, Prediction of the fluid flow heat transfer and inactivation of microorganism at medical devices in modern steam sterilizers using computational fluid dynamics, Appl. Therm. Eng. 127 (2017) 1391–1403, http://dx.doi.org/10.1016/j.applthermaleng.2017.08.085.

[7] M. Feurhuber, P. Burian, M. Magno, M. Miranda, C. Hochenauer, Development of a spatially and timely resolved CFD model of a steam sterilizer to predict the load temperature and the theoretical inactivation of bacteria based on sterilization parameters, Phys. Med. 8 (2019) 100020, http://dx.doi.org/10.1016/j.phmed.2019.100020.

[8] M. Feurhuber, P. Burian, M. Magno, M. Miranda, C. Hochenauer, CFD simulation of the inactivation of Geobacillus stearothermophilus on dental handpieces, Int. J. Heat Mass Transf. 144 (2019) 118649, http://dx.doi.org/10.1016/j.ijheatmasstransfer.2019.118649.

[9] M. Feurhuber, M. Magno, M. Miranda, C. Hochenauer, CFD investigations of steam penetration Air-Removal and Condensation Inside Hollow Loads and Cavities, Appl. Therm. Eng. 147 (2019) 1070–1082, http://dx.doi.org/10.1016/j.applthermaleng.2018.10.135.

[10] M. Feurhuber, R. Neuschwander, T. Taupitz, V. Schwarz, C. Frank, C. Hochenauer, A Computational Fluid Dynamics (CFD) model to simulate the inactivation of Geobacillus stearothermophilus spores in different moist heat sterilization environments, Phys. Med. 12 (2021) 100039, http://dx.doi.org/10.1016/j.phmed.2021.100039.

[11] M. Feurhuber, R. Neuschwander, T. Taupitz, V. Schwarz, C. Frank, C. Hochenauer, Inactivation kinetics of Geobacillus stearothermophilus spores during the sterilization in steam-NCGs (steam-air) mixtures, Phys. Med. 12 (2021) 100042, http://dx.doi.org/10.1016/j.phmed.2021.100042.

[12] M. Folezzani, M. Manfredi, G. Vignali (Eds.), CFD simulation of a retort process for food vegetable products, 2014.

[13] M. Farid, A.G. Abdul Ghani, A new computational technique for the estimation of sterilization time in canned food, Chem. Eng. Process. Process Intensification 43 (4) (2004) 523–531, http://dx.doi.org/10.1016/j.cep.2003.08.007.

[14] A. Kannan, P.G. Sandaka, Heat transfer analysis of canned food sterilization in a still retort, J. Food Eng. 88 (2) (2008) 213–228, http://dx.doi.org/10.1016/j.jfoodeng.2008.02.007.

[15] M. Cordioli, M. Rinaldi, G. Copelli, P. Casoli, D. Barbanti, Computational fluid dynamics (CFD) modelling and experimental validation of thermal processing of canned fruit salad in glass jar, J. Food Eng. 150 (2015) 62–69, http://dx.doi.org/10.1016/j.jfoodeng.2014.11.003.

[16] D. Mosna, G. Vignali, Three-dimensional cfd simulation of a steam water spray retort process for food vegetable products, Int. J. Food Eng. 11 (6) (2015) http://dx.doi.org/10.1515/ijfe-2015-0062.

[17] P.W. Cleary, Y. Serizawa, A coupled discrete droplet and SPH model for predicting spray impingement onto surfaces and into fluid pools, Appl. Math. Model. 69 (2019) 301–329, http://dx.doi.org/10.1016/j.apm.2018.12.024.

[18] F. Tahir, S.G. Al-Ghamdi, CFD analysis of evaporation heat transfer for falling films application, Energy Rep. 8 (2022) 216–223, http://dx.doi.org/10.1016/j.egyr.2021.11.096.

[19] J. Wang, X. Chen, T. Lu, X. Chen, S. Shen, B. Liu, Three-dimensional film thickness distribution of horizontal tube falling film with column flow, Appl. Therm. Eng. 154 (2019) 140–149, http://dx.doi.org/10.1016/j.applthermaleng.2019.03.041.

[20] A.A. Bhuiyan, J. Naser, Development of 3D transient wall filming mechanism during combustion by coupling Eulerian-Lagrangian approach and particle–wall interaction model, Appl. Therm. Eng. 112 (2017) 911–923, http://dx.doi.org/10.1016/j.applthermaleng.2016.10.174.

[21] H. Ding, Y. Zhang, C. Sun, Y. Yang, C. Wen, Numerical simulation of supersonic condensation flows using Eulerian-Lagrangian and Eulerian wall film models, Energy 258 (2022) 124833, http://dx.doi.org/10.1016/j.energy.2022.124833.

[22] Y. Kobashi, Y. Zama, T. Kuboyama, Modeling wall film formation and vaporization of a gasoline surrogate fuel, Int. J. Heat Mass Transfer 147 (2020) 119035, http://dx.doi.org/10.1016/j.ijheatmasstransfer.2019.119035.

[23] H. Schlichting, K. Gersten, Grenzschicht-Theorie (10), 2006.

[24] F. Moukalled, L. Mangani, M. Darwish, The Finite Volume Method in Computational Fluid Dynamics, vol. 113, Springer International Publishing, Cham, 2016, http://dx.doi.org/10.1007/978-3-319-16874-6.

[25] G.H. Yeoh, J. Tu, Computational techniques for multi-phase flows: Basics and applications / Guan Heng Yeoh and Jiyuan Tu, Butterworth-Heinemann, Oxford, 2010.

[26] A.D. Gosman, E. loannides, Aspects of Computer Simulation of Liquid-Fueled Combustors, J. Energy 7 (6) (1983) 482–490, http://dx.doi.org/10.2514/3.62687.

[27] A.M. Sterling, The Instability of Capillary Jets (Ph.D. thesis), University of Washington, Washington, 1969.

[28] A.H. Lefebvre, V.G. McDonell, Atomization and sprays, second edition Edition, CRC Press Taylor & Francis Group CRC Press is an imprint of the Taylor & Francis Group an informa business, Boca Raton, 2017.

[29] C.A. Chryssakis, D.N. Assanis, F.X. Tanner, Atomization models, in: N. Ashgriz (Ed.), Handbook of Atomization and Sprays, Springer, US, Boston, MA, 2011, pp. 215–231.

[30] M.A. Friedrich, H. Lan, J.L. Wegener, J.A. Drallmeier, B.F. Armaly, A separation criterion with experimental validation for shear-driven films in separated flows, J. Fluids Eng. 130 (5) (2008) http://dx.doi.org/10.1115/1.2907405.

[31] K.V. Meredith, J. de Vries, Y. Xin, A numerical model for partially-wetted flow of thin liquid films, in: A.A. Mammoli, C.A. Brebbia (Eds.), Computational Methods in Multiphase Flow VI WIT Transactions on Engineering Sciences, WIT PressSouthampton, UK, 2011, pp. 239–250, http://dx.doi.org/10.2495/MPF110201.

[32] J. Xu, B. Li, J. Lian, J. Ni, J. Xiao (Eds.) (Eds.), Wetting behaviors of water droplet on rough metal substrates, in: Advances in Engineering Research, vol. 93, 2016, http://dx.doi.org/10.2991/ismems-16.2016.58.

[33] D. Kuhnke, Spray wall interaction modelling by dimensionless data analysis, Berichte aus der Strömungstechnik, Shaker, Aachen, 2004.